Renewable Energy xxx (xxxx) xxx

Contents lists available at ScienceDirect

Renewable Energy

journal homepage: www.elsevier.com/locate/renene

Boundary-layer transition model for icing simulations of rotating wind turbine blades

Chankyu Son [a], Mark Kelly [a], Taeseong Kim [a, b, *]

[a] Department of Wind Energy, Technical University of Denmark, Denmark
[b] School of Mechanical, Electrical and Manufacturing Engineering, Loughborough University, UK

ARTICLE INFO

Article history:
Received 11 August 2020
Received in revised form
13 November 2020
Accepted 14 November 2020
Available online xxx

Keywords:
Flow transition
γ-Re_θ model
Surface roughness
Roughened cylinder
Reynolds-averaged Navier-Stokes equations
Wind turbine icing

ABSTRACT

Icing simulations for wind turbine blades should consider the roughness-induced flow transition. Adding a transport equation for 'roughness amplification' to the Langtry-Menter model, the roughness-induced transition can be predicted for rough flat plates. However, this approach exhibits a limitation that it cannot predict the skin friction in the shadow zone of blunt bodies. Such an approach depends on the boundary condition(s) of specific dissipation rate (ω). Typically boundary conditions for turbulent kinetic energy (k) and ω have been investigated for various roughness heights, but have been applied only for fully turbulent conditions. This study introduces an approach to predict the flow transition and the skin friction for a roughened surface, whereby the Langtry-Menter model including roughness amplification is coupled with the k and ω boundary conditions. The proposed method shows good agreement with the experiments for turbulent onset and the distributions of skin friction and heat convection for a roughened flat plate and a circular cylinder. Using the turbulent models under fully turbulent and transitional assumptions, the effects of the flow transition on the ice accretion shape on a rotating wind turbine are compared. The modified turbulent model showed better performance for the icing simulations without any tuning.

1. Introduction

Except for the tip regions, the portion of a wind turbine blade near its leading edge operates in a laminar regime, below the critical Reynolds number at which a transition from laminar to turbulent flow is expected [1]. The onset of flow transition can be changed when the blades experience icing events. It is well known that ice accretion on wind turbine blades increases surface roughness, and the surface roughness can change the transition onset [2]. The shapes of accreted ice can be determined by the flow transition induced by surface roughness, as a result of changes in pressure, skin friction, and heat transfer distributions, *i.e.*, the flow transition and ice accretion interact with each other in a non-trivial, nonlinear manner.

The flow transition induced by surface roughness occurs around the blades of operational wind turbines for a number of reasons; these include attachment of insects and/or dust, surface erosion, as well as icing. The issues related to surface roughness ('surface engineering') have been investigated extensively, both numerically and experimentally [3]. However, icing-induced flow transition is difficult to approach experimentally. Non-dimensional parameters that describe the similarity and its applicability between full-scale wind turbines and scaled models [4] have not been well-documented for icing wind tunnel tests [5,6]. At the same time, the size of modern wind turbines continues to grow [7], while icing wind tunnels that can contain contemporary wind turbine blades are not yet available. Studies of icing-induced flow transition continue to be conducted with the aid of numerical simulations and limited similarity methods [8] applied to icing wind tunnel experiments.

In the first generation of numerical icing simulation tools, led by ONERA and NASA [9], aerodynamic solutions were afforded via inviscid assumptions, as in the panel method or Euler equations with a BLT (Boundary-Layer Theory) [10,11]. BLT with consideration of surface roughness, as well as an empirical model to determine the onset of transition to turbulence [12], were then introduced into icing simulation codes [9].

BLT [10,11] has inherent limitations, including airfoils with a high angles of attack and blunt bodies. Airfoils having a high angle

* Corresponding author. Department of Wind Energy, Technical University of Denmark, Denmark.
E-mail address: tkim@dtu.dk (T. Kim).

https://doi.org/10.1016/j.renene.2020.11.070
0960-1481/

of attack, or blunt bodies such as a blade root region, generate boundary layers thicker than those for which BLT is valid. Further, the deformation of effective airfoil shape due to icing tends to trigger and enhance flow separation; thus it is difficult to apply BLT for wind turbine icing simulations. In addition, it is difficult to apply the BLT in the blade tip region, where the streamlines are no longer aligned in parallel to each other; in BLT the blade sections should be clearly divided according to (parallel) streamlines, in a way similar to blade element methods. As a result, recent icing simulation codes employ Navier-Stokes equations as the aerodynamic solver.

Direct Numerical Simulations (DNS) can explain possible mechanisms to the transition onset induced by surface roughness. Large Eddy Simulations (LES), which can be considered as a spatially-filtered model of DNS, may predict the flow transition if the sufficiently fine resolution is used. While DNS and LES compute the flow around the roughness elements directly, they require substantial computational resources. In contrast, bulk roughness characterization (starting with the equivalent sand grain approach of Nikuradse [13]) can be used to consider the mean roughness effect within the turbulence model, without resolving actual roughness elements. It uses a new parameter which increases turbulence in the wall region and the momentum transport toward the wall instead of considering each surface roughness element. Although this approach simplifies the pressure forces acting on each roughness element to be expressed via mean frictional drag, due to its efficiency it is widely used in fluids engineering to include surface roughness effects into turbulence models, such as the Spalart-Allmaras one equation model [14,15] and Menter k−ω SST model [16].

To account for the surface roughness within RANS turbulence models, the modified Spalart-Allmaras turbulence model suggested by Aupoix and Spalart [14] is generally implemented into modern icing simulation codes such as FENSAP-ICE [17], ICECREMO [18], and WISE [19] as the reference model [20]. Aupoix and Spalart [14] derived the specific boundary condition to mimic roughness effects within the Spalart-Allmaras turbulence model [15], providing the non-zero turbulent eddy viscosity (μ_t) at the wall as the boundary condition based on the effective distance $d + 0.03k_s$, where d is the distance of the first grid point from the wall and k_s, is the sand-grain roughness (see Aupoix and Spalart [14]). Since the Spalart-Allmaras model only has a single transport equation (for turbulent viscosity), it has increased computational efficiency, while yielding relatively accurate solutions for fully-turbulent conditions over rough surfaces [15]. However, the turbulent model based on the Spalart-Allmaras model was not designed to address the transition to turbulence induced by surface roughness [14].

On the other hand, the Langtry and Menter [21] transition model, known also as the γ-Re_θ model, takes the flow transition into account by modifying the k−ω SST model [16]. This model successfully predicted the aerodynamic performance of smooth two-dimensional airfoils and three-dimensional wind turbine blades [22], when flow transitions occur. To consider the surface roughness, the transport equations and boundary conditions have been studied based on the Langtry-Menter transition model [21].

To treat the effect of surface roughness on the turbulence transition of boundary-layer flow, a transport equation of a variable called 'roughness amplification' (A_r) was added to the Langtry-Menter transition model [21] by Dassler et al. [23]. Thereafter, Langel et al. [24] generalized the roughness amplification method through a blending function to prevent unphysical undershoots in the transition onset criterion. They improved the boundary condition for A_r from an analytical solution. Both studies [23,24] employed the boundary condition value for the specific dissipation rate (ω) suggested by Wilcox [25]; but, this requires very fine near-wall mesh resolution [26,27]. Dassler et al. [21] and Langel et al. [24] validated their methods only for flow past a flat plate. However, for transitionally and fully rough surfaces, predictions for skin friction are unsatisfactory because the Wilcox [25] boundary condition is that of vanishing turbulent kinetic energy (k) and eddy viscosity (μ_t) through the surface, independent of the roughness height. As a result, Dassler et al. [21] and Langel et al. [24] underestimate the skin friction in the turbulent and fully roughened surface region.

Various works accurately account for the surface roughness within RANS turbulence models through the implementation of the boundary conditions. Durbin et al. [28] developed the k boundary conditions applicable to fully roughened surfaces for the k-ε turbulence model. For fully rough conditions, the viscous sublayer is disturbed. The mean velocity follows a logarithmic profile but with a certain amount of displacement, which is determined by experimental correlation using skin friction and momentum thickness on the roughened flat plate. Non-zero values of k and μ_t at the wall were then calculated from the log-law solution. Knopp et al. [29] extended the boundary conditions for k and ω, using the k boundary condition of Durbin et al. [21]. Since Aupoix and Spalart [14] presented a method to calculate μ_t directly according to surface roughness length, then ω could be determined by the definition for the k-ω SST turbulence model: $\mu_t = k/\omega$. Aupoix [30] later found that the Knopp et al. [29] model performed well over the fully rough surface (for $k_s^+ > 100$), but underestimated the displacement of the velocity profile for transitionally rough surfaces. He modified the correlation equations for the k and ω wall boundary values from the experimental data instead of using the log-law solution. Furthermore, he applied a reference coordinate system shifted by $0.03k_s$ toward the wall in the governing equations of the k-ω SST model, as carried out by Aupoix and Spalart [14] for the baseline Spalart-Allmaras model [15].

The governing equations or boundary conditions have been modified in various works to account for surface roughness effects in RANS turbulence models. Langel et al. [24] added a transport equation of roughness amplification to the Langtry-Menter transition model to accurately predict the transition onset over various roughness lengths. The transition onset positions of roughened plates were validated against experimental data. However, the distributions of skin friction on airfoils or other two-dimensional bodies have not been verified yet, because Langel et al. [24] retains Wilcox's boundary conditions [25] only for ω. Consequently, the wall value for μ_t cannot be defined on the leeward side of bodies, i.e. within the so-called shadow zone. On the other hand, Knopp et al. [29] derived the boundary conditions for the k and ω for various roughness height. Their study could not predict the flow transition because their boundary conditions were applied under the fully turbulent assumption and only validated for roughened flat plates.

Although the flow transition induced by the surface roughness should be considered for the wind turbine icing simulations [22], wind turbine icing simulations were spun-off from aircraft icing simulation codes. Since most of the aircraft operates above the critical Reynolds number, the fully turbulent assumption was valid. However, the wind turbine simulations require the ability to predict the flow transition which can determine the ice accretion shapes and aerodynamic performance of blades. In addition, the transition model has to consider the surface roughness effect to implement into icing simulations, because the surface roughness due to icing accelerates the flow transition. However, there is not (yet) a turbulent model in the literature to accurately predict the heat transfer and skin friction for flows past wind turbine blades including ice accretion where the flow transition is induced by the surface roughness.

Unlike previous studies that only modify boundary conditions [29] or transport equations [24], this study simultaneously

combined the transport equations and boundary conditions for the turbulent model in order to predict the flow transition and the distributions of skin friction for the roughened surface. Based on the model suggested by Langel et al. [24] which modifies the transport equations from the Langtry-Menter transition model [23], the boundary conditions derived by are Knopp et al. [29] are applied. The transport equations are introduced in section 2.2. The boundary conditions are described in section 2.3. The newly coupled turbulent model validated against the experimental data which provides transition onsets and distributions of skin friction on the roughened flat plate in section 3.1 and circular cylinder in section 3.2, as well.

The validated turbulent model is implemented into the 3D icing simulation code WISE (Wind turbine Icing Simulation code with performance Evaluation) [19]. Based on the RANS equations, WISE is also descended from an aircraft icing code, as is the case with other icing simulation tools for wind turbines [17,31–33]. To extend from an aircraft to a wind turbine icing simulation tool, the moving reference frame was applied in a consistent manner for both aerodynamic and water droplet fields. The modified Spalart-Allmaras [14] turbulence model was also employed, under the fully turbulent assumption. Consequently, this study aims to confirm the necessity of applying a turbulent model that can account for the flow transition induced by surface roughness in the wind turbine icing simulation. By implementing two different turbulence models into WISE, the fully turbulent model and flow-transition model, the contrast of ice accretion shapes on rotating wind turbine blades is examined in section 3.3. In addition, the distributions of the heat transfer rate and skin friction that determine the ice accretion shapes are systematically analyzed.

2. Methods

2.1. Wind turbine icing simulation code with performance evaluation (WISE)

By faithfully considering the blade rotation effect, the fixed-wing aircraft icing tool named ISEPAC [34,35] (Ice Shape Evaluation and Performance Analysis Code) is extended to WISE [19] as the simulation tool for wind turbine icing. Fig. 1 shows the structure of WISE, which has four main modules, namely the: 1) aerodynamic module, 2) droplet field module, 3) thermodynamic module, and 4) grid-regeneration module. The MRF (Moving Reference Frame) method in both flow analysis and droplet-trajectory calculation modes is applied. In the thermodynamic module, the motion of thin water film is obtained by the flow analysis module where the MRF method is applied. The total icing exposure time is divided into several intervals. For a given time interval, four modules progress sequentially under the steady-state assumption. The grid-regeneration module updates the ice accumulated surface grid, with the volume grid generated by an external tool. The newly updated grid can be the initial condition for the next time interval. The final ice shape can be obtained by repeating a series of processes several times.

A minor improvement is applied for the thermodynamic module in this study. The phase change of impinging water (from water to ice) is analyzed by a thermodynamic module. The flow of unfrozen water is also determined in this module. For high-speed conditions (e.g. for aircraft wings), the viscosity-related heating prevents ice accretion near the freezing temperature. Below freezing temperature, the effect of convective cooling is much larger than that of evaporation. On the contrary, the power curves of wind turbines have been observed to be somewhat lower than ideal above the freezing temperature [36]. Due to the lower velocity of wind turbine blades compared to aircraft wings, the effect of evaporation is relatively larger than for aircraft wings. Thus terms related to evaporation are added to the mass and energy conservation equations of the thermodynamic module in WISE:

$$\rho_w\left[\int\frac{\partial h_f}{\partial t}dV+\int\nabla\cdot\left(h_f\overline{U}_f\right)dV\right]=\dot{m}_{\mathrm{com}}-\dot{m}_{\mathrm{ice}}-\dot{m}_{\mathrm{evap}} \tag{1}$$

and

$$\begin{aligned}\rho_w\left[\int\frac{\partial h_f C_{p,w}\tilde{T}_{eq}}{\partial t}dV+\int\nabla\cdot\left(h_f C_{p,w}\tilde{T}_{eq}\overline{U}_f\right)dV\right]\\ =\dot{m}_{\mathrm{com}}\left[C_{p,w}\tilde{T}_\infty+\frac{1}{2}U_{d,r}^2\right]+\dot{m}_{\mathrm{ice}}\left[L_{\mathrm{fus}}-C_{p,i}\tilde{T}_{eq}\right]\\ -h_c(T_{eq}-T_\infty)-\dot{m}_{\mathrm{evap}}\left[C_{p,w}\tilde{T}_{eq}+L_{\mathrm{vap}}\right].\end{aligned} \tag{2}$$

Here h_f and $\overline{U}_f$ are the thickness and velocity of water film on the blade, $\dot{m}_{\mathrm{com}}$ is the flow rate per unit area of impinging water, $\dot{m}_{\mathrm{ice}}$ is the ice accretion rate, $\tilde{T}_{eq}$ is the equilibrium surface temperature, $\tilde{T}_\infty$ is the incoming droplet temperature in Celsius, $U_{d,r}$ is the relative droplet velocity, ρ_w is the liquid water density, $c_{p,w}$ is the water heat capacity, h_c is the heat convection coefficient, L_{fus} is the latent heat of fusion, L_{vap} is the latent heat of vaporization, and T_∞ is the incoming air temperature in Kelvin. The evaporative mass flux is calculated based on boundary-layer theory [11], as

$$\dot{m}_{\mathrm{evap}}=\frac{0.622h_c}{C_{p,a}}\left(\frac{p_{\mathrm{sat}}|_w-p_{\mathrm{sat}}|_e}{p_e-p_{\mathrm{sat}}|_w}\right). \tag{3}$$

In Eq. (3) the saturated vapor pressure p_{sat} is obtained by the formula suggested by Huang [37]. The subscripts w and e denote evaluation at the wall and edge of the boundary layer, respectively; p_e is the edge pressure of the boundary layer.

The ice shapes are explicitly calculated from the evaluation of the ice mass accreted on the surface. An updated grid is generated for the next step calculation from the grid-regeneration module. The ice thickness can be calculated from the mass of freezing ice by dividing by the ice density. This process is repeated with the newly updated ice accretion shape which obtained steady-state assumption.

Each module was systematically validated against experiments and/or state-of-the-art numerical simulations. Ice accretion shapes on 2D airfoils, 3D aircraft, and helicopter fuselage (such as non-rotating applications obtained by ISEPAC [34,35], which is the predecessor of WISE) were validated against icing wind tunnel and numerical simulations. Due to the absence of reliable ice accretion shapes for the rotating wind turbines obtained in icing wind tunnels, each module was systematically validated against experiments or compared with state-of-the-art numerical simulations. The aerodynamic module based on the MRF method for a rotating wind turbine was validated against the wind tunnel test and numerical simulations. The droplet field module, which also employs the MRF method, was verified by comparing the ice accretion shapes with FENSPA-ICE under a rime ice condition. Due to the extremely low temperature, the effects of the thermodynamic module can be excluded from the icing simulation. To verify the thermodynamic module, the ice accretion shapes obtained by WISE and FENSAP-ICE under a glaze ice condition are compared. Details about WISE and validation results can be found in our previous study [19].

In the previous study, WISE employed the modified Spalart-Allmaras turbulence model [14] to take into account for the surface roughness-induced by ice accretions under the fully turbulent assumption. The modified Spalart-Allmaras model mentioned in the introduction section was implemented into WISE. As revealed

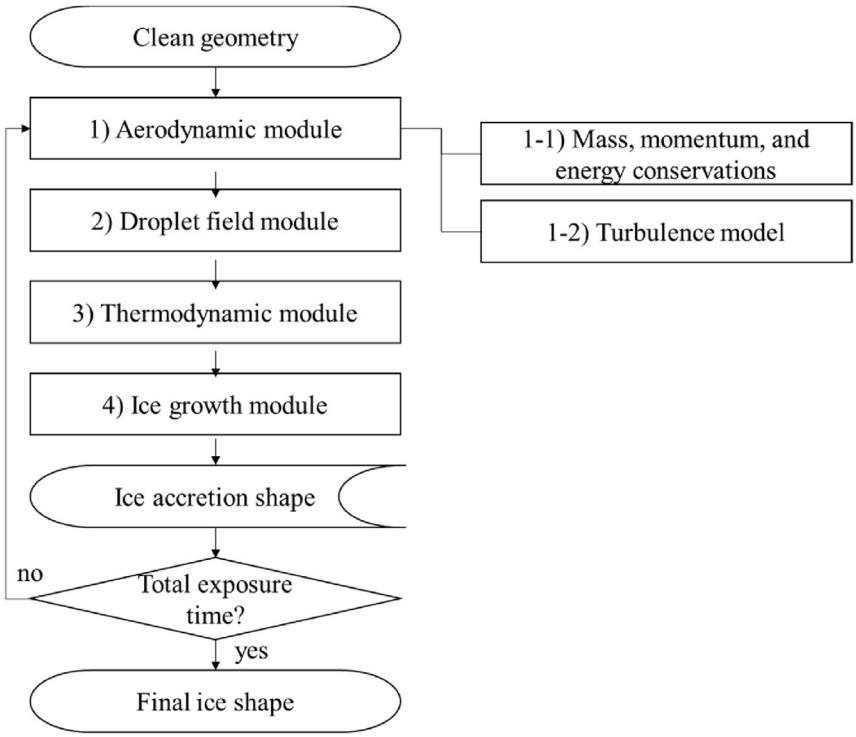

Fig. 1. Flowchart of the developed code.

in the study of Langtry [1], it is essential to apply the transition model for wind turbines. Therefore the present study applies the flow transition model to wind turbine icing simulation. In order to effectively consider the flow transition due to the surface roughness, a modified transitional transport equation for roughness amplifier (section 2.2) and associated boundary conditions (section 2.3) are applied.

2.2. Transition model

The newly developed transition model in this study is implemented in WISE to consider the flow transition induced by surface roughness. The transition model follows the method suggested by Langel et al. [24], which has been successfully verified for flow past a roughened flat plate. Langel et al. [24] added an additional transport equation for roughness amplifier (A_r)

$$\frac{\partial(\rho A_r)}{\partial t}+\frac{\partial(\rho U_j A_r)}{\partial x_j}=\frac{\partial}{\partial x_j}\left[\sigma_{ar}(\mu+\mu_t)\frac{\partial A_r}{\partial x_j}\right], \tag{4}$$

to the turbulence model; it can account for the transition to turbulence suggested by Langtry and Menter [21]. The roughness is considered within the boundary condition of A_r, which is a function of the non-dimensional sand-grain roughness k_s^+:

$$A_r|_{wall}=c_{r1}{k_s}^+. \tag{5}$$

The roughness amplification initiates the transition process by increasing the Reynolds number of the local momentum thickness, effectively triggering an earlier transition according to the surface roughness. This is done through an additional transport equation within the Langtry and Menter (γ-Re_θ) model, which parameterizes the Reynolds number of the transition onset momentum thickness ($\widetilde{Re}_{\theta_t}$); A_r acts to decrease the production term

$$\tilde{P}_{\theta_t}=c_{\theta_t}\frac{\rho}{t}\left[\left(Re_{\theta_t}-\widetilde{Re}_{\theta_t}\right)(1-F_{\theta_t})-F_bF_{A_r}\right] \tag{6}$$

in the transport equation for $\widetilde{Re}_{\theta_t}$,

$$\frac{\partial(\rho\widetilde{Re}_{\theta_t})}{\partial t}+\frac{\partial(\rho U_j\widetilde{Re}_{\theta_t})}{\partial x_j}=\tilde{P}_{\theta_t}+\frac{\partial}{\partial x_j}\left[\sigma_{\theta_t}\frac{\partial\widetilde{Re}_{\theta_t}}{\partial x_j}\right]. \tag{7}$$

The decrease in production is accomplished through a blending function F_{A_r}

$$F_{A_r}=\begin{cases} c_{r2}\cdot A_r^3 & : A_r<C_{Ar} \\ c_{r2}(A_r-C_{Ar})+c_{r2}C_{Ar}^3 & : A_r\geq C_{Ar}\end{cases}, \tag{8}$$

where

$$C_{Ar}=\sqrt{c_{r3}/2c_{r2}}. \tag{9}$$

The factor F_b, with F_{A_r} in (6) enforces a prescribed minimum value of $\widetilde{Re}_{\theta_t}$ in (7). The model constants for the transport equation are as follows:

$$c_{r1}=8 \quad c_{r2}=0.0005 \quad c_{r3}=2 \quad \sigma_{ar}=10 \quad \sigma_{\theta_t}=2 \quad c_{\theta_t}=0.03. \tag{10}$$

The subsequent procedure is the same as for the Langtry and Menter (γ-Re_θ) model [21]. The modified $\widetilde{Re}_{\theta_t}$ in Eq. (7) is applied for the production terms of the intermittency (γ) transport equitation. The turbulent kinetic energy (k) can be scaled according to the local intermittency value. Detailed information on this roughness amplification model can be found in Langel et al. [24].

2.3. Wall roughness boundary conditions

Previous transition models employing the roughness amplifier [23,24] used the boundary condition suggested by Wilcox [25]. For the rough surface, the value of specific dissipation rate at the wall had been prescribed as

$$\omega_{\text{wall}} = \frac{u_\tau^2 S_R}{\upsilon}, \tag{11}$$

where u_τ is the friction velocity and the non-dimensional function S_R was defined by

$$S_R = \begin{cases} \left(\dfrac{50}{k_s^+}\right)^2 & : k_s^+ \le 25 \\ \dfrac{100}{k_s^+} & : k_s^+ > 25\ . \end{cases} \tag{12}$$

However, the skin friction is not accurately predicted with this boundary condition, because the Wilcox [25] model keeps $k = 0$ and $\mu_t = 0$ at the wall. The original SST limiter was designed for smooth surfaces, which have a viscous sublayer. However, the viscous sublayer in such a model does not consider the state of the surface, because it does not vanish over fully rough surfaces; therefore the original SST limiter becomes inappropriate over transitionally rough or fully rough surfaces. To consider roughened surfaces, Hellsten and Laine [38] modified the SST limiter by adding the function

$$F_3 = 1 - \tanh\left[\left(\frac{150\upsilon}{\omega d^2}\right)^4\right] \tag{13}$$

to the SST limiter

$$\mu_t = \frac{a_1 \rho k}{\max(a_1\omega; |\Omega| F_2 F_3)}, \tag{14}$$

where d is the distance to the nearest wall-point, the constant a_1 is 0.31, and Ω is vorticity. The value of F_3 is zero in the near-wall region and unity elsewhere, as seen in Eq. (13). Consequently, the F_3 term prevents activation of the original SST limiter above the transitionally rough or fully rough surfaces.

The equivalent sand grain approach suggested by Nikuradse [13] explained the disappearance of the viscous sublayer as increasing the μ_t near the wall regions. Since the μ_t can be determined by the k *and* ω values as written in Eq. (14), a specific nonzero value for k should be considered. The wall value of k proposed by Knopp et al. [29] is

$$k_{wall} = k_{rough}\varphi_{r1} \quad k_{rough} = \frac{u_\tau^2}{\sqrt{\beta_k}} \quad \varphi_{r1} = min\left(1, \frac{k_s^+}{90}\right), \tag{15}$$

where k value at the wall should be close to the log-layer value. Thus k_{rough} was suggested by Durbin et al. [28] based on the log-layer value. However, the log-layer value is only valid for the fully roughened condition, and Durbin et al. [28] assumed that the k value linearly varies according to the roughness height (k_s^+); this is consistent with the blending function, φ_{r1}. Consequently, the proper k value is introduced at the wall (k_{wall}) for the smooth and transitional rough surface, as well as for the fully rough surface.

This model has the advantage of being applicable to the transition model. Even if the surface has uniform roughness, there is a viscous sublayer near the stagnation region where the laminar flow is maintained. The blending function φ_{r1} prevents unintentional flow transition due to the rapid growth of k_{wall} and μ_t in laminar regions, which have a hydraulically smooth or transitionally roughened surface.

The ω boundary condition is also modified, through

$$\omega_{wall} = \frac{u_\tau}{\kappa \tilde{d}_0 \sqrt{\beta_k}}, \tag{16}$$

where

$$\tilde{d}_0 = \varphi_{r2} 0.03 k_s \tag{17}$$

and

$$\varphi_{r2} = \min\left[1, (k_s^+/30)^{2/3}\right] \min\left[1, (k_s^+/45)^{1/4}\right] \min\left[1, (k_s^+/60)^{1/4}\right]. \tag{18}$$

By definition for the k-ω SST turbulence model under fully rough conditions, $\mu_t = k/\omega$, Eq. (14) can be derived. Eqns. (16)-(18) explain the velocity shift $\Delta u/u_\tau$ and skin friction for transitionally and fully roughened surfaces. The $\tilde{d}_0$ value in Eq. (17) plays the same role as the effective distance due to the surface roughness in the Spalart-Allmaras turbulence model suggested by Aupoix and Spalart [14]. The ω boundary condition implementation also adopts the blending function φ_{r2} (see Eq. (18)) to explain the transitional and fully rough surface, since Eq. (16) is valid under fully rough conditions. The blending function φ_{r2} is calibrated to fit the experimental skin friction on the flat plate [39].

Aupoix [30] pointed out the underestimation of the velocity shift $\Delta u/u_\tau$ in the transitionally roughened surface with Knopp et al. [29] model. He modified the correlation equation for the k and ω wall values using the experimental data of Colebrook and White [40], where the effective distance ($d + 0.03k_s$) is applied to account for surface roughness in the governing equations of the k-ω SST turbulent model. The specific value of 3% of roughness height ($0.03k_s$) was derived to be consistent with two fundamental regimes: the fully roughened velocity profile [13], and infinite roughness height ($k_s^+ \to \infty$) [41]. However, applying the Aupoix [30] method to the present study—treating the flow transition—introduces very large perturbations and large μ_t (even in the laminar flow region), due to the effective roughness wall distance. As a result, it induces premature flow transitions regardless of the roughness height and Reynolds numbers. Thus, Knopp's model is applied to prevent too high perturbations by the roughness in the laminar region.

The present method is implemented into OpenFOAM® as the independent turbulence model and boundary conditions. The present method uses the Langtry-Menter [21] transition model coupled with the roughness amplifier (A_r) in Eq. (4) suggested by Langel et al. [24]. The modified SST limiter suggested by Hellsten and Laine [38] is applied as well. As the boundary conditions for k and ω, the present method adopts the Knopp et al. [29] method. To clearly show the difference between the present method and that of Langel et al. [24], the latter is also implemented into OpenFOAM®. Here, the ω boundary condition of Wilcox [25] is adopted keeping $k = 0$ at the wall without the modified SST limiter by following the suggestion of Langel et al. [24].

To verify the implementation of the present method and the Langel et al. [24] method ('Langel' in OpenFOAM), roughened flat plate cases are simulated and compared. To evaluate the improvement of the present method, distributions of skin friction on a roughened circular cylinder are compared with the Langel-model results in OpenFOAM and with experimental results.

The results include ice accretion shapes, found on blades of the

NREL Phase VI turbine; these are obtained from both fully turbulent and transitional models. The NREL phase VI is a two-bladed rotor, with each blade having a 5 *m* span. The tapered and twisted blades are based on the S809 airfoil described by Zanon et al. [42]. The wind speed and rotation rate are 7 m/s and 72 rpm, respectively (the tip speed ratio is 5.4). Although the NREL Phase VI rotor is a scaled model that has a short span of 5 m, the Reynolds number at the tip is similar to that of a full-scale MW class wind turbine because of its high rotational speed. The ambient condition to simulate glaze ice is chosen. The ambient temperature is 270.15 K; LWC is 0.5 g/m^3; median-volume diameter (MVD) is 20 μm; and icing exposure time is 60 min. 5.5 million grid cells are used with a cylindrical computational domain.

3. Results and discussion

3.1. Roughened surface

The verification of the roughness model is performed with the roughened flat plate test of Feindt [43] used in the validation of the roughness amplifier model by Dassler et al. [23]. Unfortunately, the experimental data of Feindt [43] were not directly accessible; this study relies on the information provided by Dassler et al. [23] and Langel et al. [24].

Numerical simulations are performed under the distance-based Reynolds number ($Re = \rho U x/\mu$) of 1.3×10^6, where x is the distance from the leading edge of the plate. The freestream velocity is set to be 15 m/s. At the plate length of 1.3 m, Re_x reaches the target value. To minimize the effects of the outflow boundary as the zero pressure gradient condition, 2 m of flat plate length is applied. The turbulent freestream intensity of 0.9% is used following the simulation of Langel et al. [24].

Fig. 2 shows the modeled and experimental values of transition onset Reynolds numbers (Re_{xt}), versus the equivalent sand-grain roughness length Reynolds number ($Re_{ks} = \rho U k_s/\mu$). The results from various numerical simulations of Dassler et al. [23] and Langel et al. [24] using a roughness amplifier are depicted with the measured data by Feindt [43]. The present method predicts transition onset position, consistent with the other numerical results as well as the experiments.

Fig. 3 shows the skin friction (coefficient, $\tau_w/0.5\rho U_\infty^2$) along the flat plate surface with various roughness Reynolds numbers; this includes the results of Langel et al. [24] and the implementation of their model into OpenFOAM (circular points and dashed lines, respectively), and the present method (solid lines). As expected, the transition onset locations, where the skin friction soars, move toward the freestream for increased roughness lengths (in all simulations). As already shown in Fig. 2, the transition locations of the present method matched with those of Langel et al. [24]. The skin

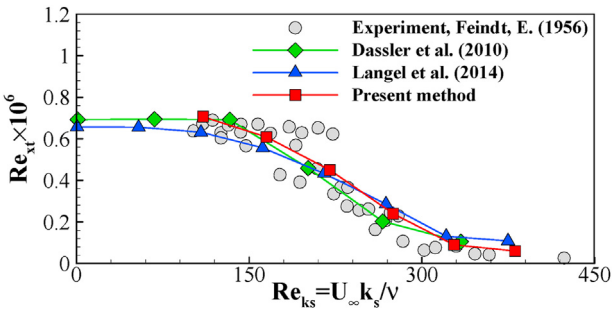

Fig. 2. Transition onset position with various roughness heights.

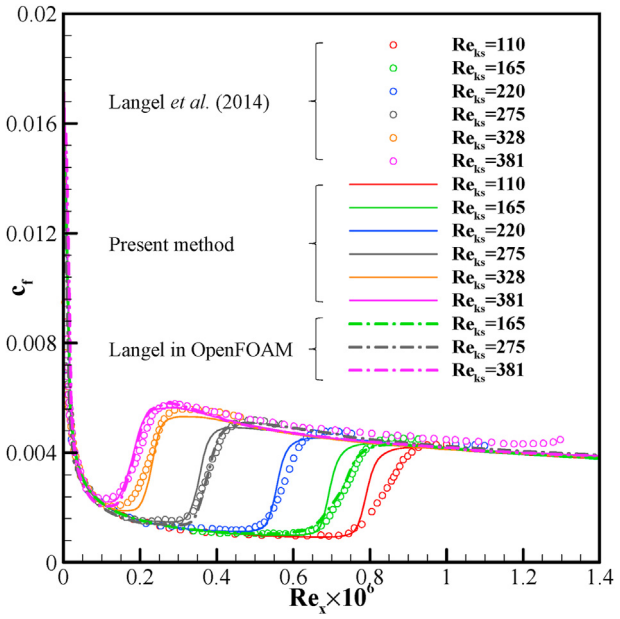

Fig. 3. Skin friction coefficient with various roughness heights.

frictions of Langel et al. [24] and the present method are well-matched in both the laminar and turbulent regions. The most noticeable thing is the slope of skin-friction spikes. The blending function φ_{r1} for k and the small value of transition intermittency (γ), which is coupled as a source term in the k equation, leads to small values of k in the laminar region. Since the μ_t is determined there by the ratio of k and ω as shown in Eq. (14), the k and μ_t are small in the laminar region. Consequently, the skin frictions of the present method and the method using $k = 0$ at the wall are not different in the laminar region. On the other hand, the k, γ, and μ_t tend to increase at the same time in the transition region. Because of the rapid increase in γ and μ_t predicted by the present method, the slope of skin friction is sharp in the transition region. Although the present method used the boundary conditions designed for fully turbulent assumption, it was confirmed that unintended roughness-induced perturbations were suppressed in the laminar region due to the blending functions of k and boundary conditions on ω.

The method suggested by Langel et al. [24] was implemented into OpenFOAM, without giving deviations from the original work. For the roughened flat plate in Fig. 3, the Langel et al. [24] results (symbols) and their methods implemented in OpenFOAM (dashed lines) are identical. To demonstrate the improvement of the present method, the skin frictions on the roughened circular cylinder obtained by the present method, Langel's methods in OpenFOAM, and the wind tunnel test will be compared in the next section.

3.2. Roughened circular cylinder

Achenbach [44] performed an experimental study to investigate the influence of surface roughness on the cross-flow around a circular cylinder. Using a high-pressure wind tunnel and skin friction probes, he obtained local skin friction distribution, transition onset position, and the location of boundary layer separation for various Re and Re_{ks}. A circular cylinder with diameter $D = 0.15$ m and span of 0.5 m was used for their experiment. The non-dimensionalized equivalent sand-grain roughness (k_sD) was 110×10^{-5}. The ambient temperature was fixed at 60 °C using a low-speed pressurized wind tunnel. Achenbach [44] mentioned that his results included the wall effect because the size of the test section

($0.5 \times 0.9\ m$) was small compared to the cylinder diameter. Thus, the two-dimensional numerical simulations are performed with the test section as smooth walls in this study.

To clearly show the improvement and limitation of the present turbulent model, simulations are performed for various Reynolds numbers from laminar, flow transition, and turbulent conditions. Fig. 4 shows the skin friction distributions obtained by the present method (solid line), Langel's model in OpenFOAM (dashed line), and Achenbach's experiment (symbol) along with the roughened cylinder for the relatively smooth surface, $k_s/D = 110 \times 10^{-5}$.

For the flat plate, there were no big discrepancies between the present and Langel's methods. There is only the difference in slopes of skin friction spike for $Re_{ks} \leq 165$. The transition onset position and overall distributions of skin friction in the laminar and turbulent region are almost identical. However, the results of the present method and Langel's methods in OpenFOAM have two remarkable differences in skin frictions for the roughened cylinder at high Reynolds numbers. As shown in Fig. 4, the transition position and the peak of skin friction of both numerical results are notable. Firstly, the present method accurately predicts the distribution and peak of skin frictions at $Re = 4.3 \times 10^5$ and $Re = 6.5 \times 10^5$. Unlike the flat plate, the jump in μ_t in the wake region of the cylinder cannot be ignored. The increased k and μ_t over the fully roughened and turbulent surface yield good agreement with the experimental data. Secondly, the transition onset position of the present method is predicted more accurately than that of Langel's methods in OpenFOAM. The experiment shows the transition point is at $\theta = 40°$ for $Re = 4.3 \times 10^5$ and $\theta = 26°$ for $Re = 6.5 \times 10^5$, respectively. The present method predicts the transition point at $\theta = 54°$ for $Re = 4.3 \times 10^5$ and $\theta = 33°$ for $Re = 6.5 \times 10^5$, respectively. However, the transition points are impeded for $Re = 4.3 \times 10^5$ and $Re = 6.5 \times 10^5$ by Langel's methods in OpenFOAM. As shown in Fig. 3, in the transition region the slope of skin friction for the present method is higher than that of Langel et al.'s model implemented into OpenFOAM. The increased k and μ_t in the present method induce the slightly early transition for the roughened cylinder case.

The main reason that the present method slightly overestimates the skin friction for the lower Reynolds number is that the boundary conditions used in the present method and Langel et al.'s model are both derived with the fully turbulent assumption. Therefore modification Eq. (5) for the roughness amplifier (or its boundary condition) is required to improve the accuracy in purely laminar flow.

When the impinging water freezes, latent heat is released. Since advection takes most of the released latent heat, the ice accretion shapes can be determined according to the distributions of heat transfer rate. In particular, the ice horn, the distinctive characteristic of ice shape in glaze conditions, occurs mainly at the peak of heat transfer. The location, length, and growth direction of the ice horn depend on the value and position of the peak of the convective cooling. Thus the turbulent model has to predict the overall heat transfer distributions, as well as the peak of convective cooling.

To confirm that the present turbulent model is suitable for icing simulations, the distribution of heat transfer rates is validated against the experimental data [45]. The distributions of heat transfer were obtained in the same experimental arrangement and measurement techniques as the experiment [46] that obtained the distributions of skin friction according to the surface roughness and Reynolds number shown in Fig. 5. To keep a constant surface temperature, the cylinder in the experiment was made of copper, which has a high thermal conductivity [45]. In consideration of the surface material, the constant surface temperature was prescribed in the numerical simulations; also following the experiment, the laminar Prandtl number (Pr_l) is set to 0.72 in the numerical simulation. In the numerical simulation, the constant turbulent Prandtl number (Pr_t) is applied as 1.0. To accurately predict the heat transfer rate for transitional flow, a few studies have correlated the local Pr_t with the roughened flat plate with fully turbulent conditions [47,48]. The validity of correlated Pr_t for the flow transition model is not yet unveiled. In this study, the thermal diffusivity was calculated by definition of heat transfer analysis, instead of applying correlation to adjust unknown Pr_t.

The distributions of Frossling number ($Fro = Nu/\sqrt{Re}$) with various roughness heights on the circular cylinder are plotted in Fig. 5. At $Re = 2.2 \times 10^5$, the experiment shows that flow past the

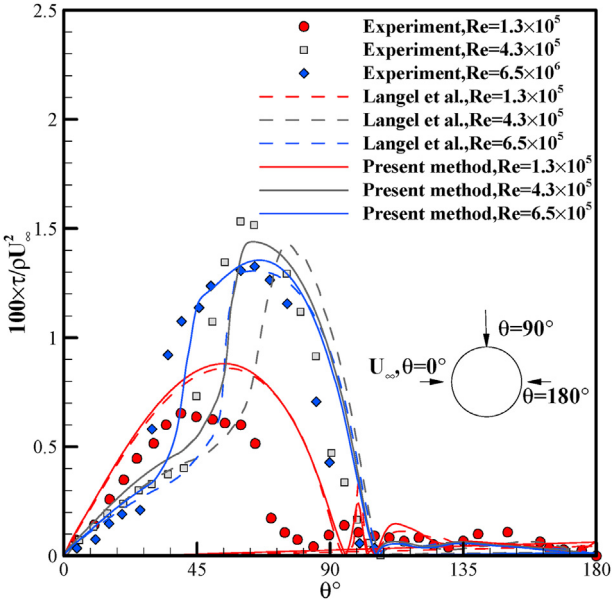

Fig. 4. Distributions of skin friction for the roughened circular cylinder ($k_s/D = 110 \times 10^{-5}$).

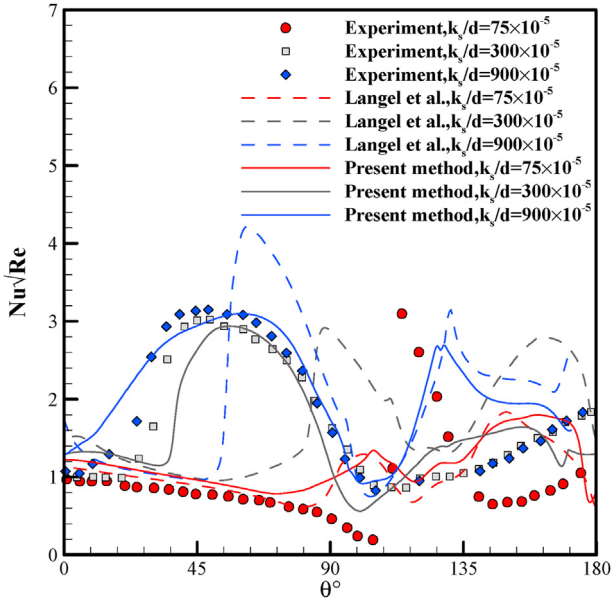

Fig. 5. Distributions of Frossling number ($Fro = Nu/\sqrt{Re}$) on the roughened circular cylinder ($Re = 2.2 \times 10^5$, $Pr_l = 0.72$).

smooth surface ($k_s/D = 75 \times 10^{-5}$) is still subcritical. Both the present method and Langel's in OpenFOAM also predict the flow as laminar. A substantial increase of the *Fro* can be observed due to the laminar separation in the experiment. However, the reduced *Fro* at the separation region is calculated by the time-averaged numerical simulations. At $k_s/D = 300 \times 10^{-5}$, the laminar-turbulent transition occurs about $\theta = 27^{\circ}$ in the experiment. It is consistent with the result of skin friction shown in Figs. 4 and 5. The turbulent flow is found for the cylinders with the highest roughness case for both results of the experiment and the present method. The peak and overall distribution of *Fro* obtained by the present method are well-matched with the experimental data under various roughness height. In contrast, the transition onsets are impeded for both cases of $k_s/D = 300 \times 10^{-5}$ and 900×10^{-5} when Langel et al.'s model is applied. Regardless of the roughness heights, the transition onset is shifted to about 45° down-stream. Langel et al.'s model shows the limitations to capture the distributions and peak values.

One thing to be improved from the current method is that the transition onset is somewhat impeded. It is discovered that nonzero k at the wall and the roughness amplifier (A_r) can trigger early onset of transition. As a result the present method accurately predicts the distributions of skin friction and heat transfer rate without any modifications to the transport equation or boundary conditions—regardless of the application (e.g. flat plate or circular cylinder).

In addition, the overall distributions and peaks of both skin friction and *Fro* are well predicted against the experiment. The blending function (φ_{r1}) for k in Eq. (15) is linearly correlated as a monotonic function of k_s^+ because it was derived from the flat plate with critical Reynolds numbers. If this blending function becomes more elaborate and/or certain based on the accumulation of more experiments, the accuracy of the transition onset will be improved. The other thing to note is that the present method predicts the distributions of *Fro* on the circular cylinder without correlating the Pr_t.

3.3. Ice accretion shapes

The ice accretion shapes on NREL phase VI blades are predicted by using WISE with the suggested turbulent model. The freestream velocity of 7 m/s, LWC of 0.5 g/m^3, MVD of 20 μm, icing exposure time of 30 min, and temperature of 270.15 K are considered, respectively. The tip speed ratio is 5.4. The single-shot icing computational strategy is applied, without the surface smoothing procedure in the ice-growth module in this study. although WISE is able to consider the multi-shot method [19]; this is because the single-shot method significantly reduces computational cost compared to the multi-shot method. Furthermore, it was revealed that there were no dramatic differences in ice shapes, such as horns, in previous studies using FENSAP-ICE and WISE [17,19].

The number of grid points in each blade section is roughly 100−120, with the number of grid points per area decreasing toward the outboard. The absence of surface smoothing of ice accretion shapes, and the relatively small number of grid points on the outboard, can yield a large angular ice shape; however, these modeling choices are sufficient to capture the maximum ice thickness, ice growth direction, and icing limits. To capture the velocity profile near walls, ten prism layers with a growth rate of 1.2 are applied, and with wall y^+ values kept below 5—equivalent to the y^+ values applied to predict the skin friction on the cylinder shown in Figs. 4 and 5. About 6 million grid cells are used with a three-dimensional cylindrical computational domain. More details about the grid system are described in Ref. [19].

To determine the surface roughness, various models were suggested. The roughness models based on the ambient meteorological parameters proposed in LEWICE [49] and freezing fraction modified in LEWICE 3.2 [50] are practical. In LEWICE 3.2 [50], the surface roughness can be determined as a function of the freezing fraction at the stagnation point. However, the roughness model based on the freezing fraction has a few limitations. First, it is difficult to define a stagnation point or line on a 3D blade, such as in the tip region where the 3D effect cannot be ignored. Second, it requires tremendous computational resources. To obtain the converged freezing fraction and surface roughness, several iterations are required through the aerodynamic, droplet field, and thermodynamic modules. These iterative calculations are a computational burden for 3D icing simulations, even when the single-shot method is applied to obtain the ice accretion shape.

Due to the aforementioned disadvantages of the roughness model based on the freezing fraction, in our study we applied the surface roughness model suggested by LEWICE [49]. The surface roughness can be determined as the function of the ambient temperature, LWC, MVD, and velocity. The sectional surface roughness varies in the spanwise direction, as the sectional velocity increases linearly. Although a constant non-dimensionalized surface roughness ($k_s/D = 95 \times 10^{-5}$), which is taken at $r/R = 75\%$, is applied for the entire blade as the reference value, the k_s/D matches the mid- and tip sections to within 8%. Since the surface roughness model only requires an ambient meteorological parameter, the surface roughness can advantageously be determined as initial input to the simulation without any iterative calculations.

Fig. 6 shows the ice accretion shapes on NREL phase VI blades, at three different spanwise positions; results from the fully turbulent (modified Spalart-Allmaras) model, the new method developed here (transitional model), and the FENSAP-ICE model (modified Spalart-Allmaras with a trip term) are compared. It is clearly seen that our proposed transitional method very well predicts the icing limit on the upper surface compared to FENSAP-ICE, while the fully turbulent model underpredicts the icing limit significantly. For example, the suggested turbulent model and FENSAP-ICE predict the upper limit on $s/c = 0.049$ and 0.064, while the fully turbulent model underpredicts the upper limit on $s/c = 0.029$ and 0.036 at r/R of 46.7% and 63.3%, respectively. Here, c is the sectional chord length, and s is the distance from the stagnation point marked with circles in Fig. 6. Negative s means lower surface. In the tip region at $r/R = 80.0\%$, the discrepancy is getting bigger between the current turbulent model and the fully turbulent model. The discrepancies of the icing limit on the lower surface are even larger between the fully turbulent model, the proposed turbulent model, and FENSAP-ICE as it is shown in Fig. 6.

FENSAP-ICE used the modified Spalart-Allmaras model with a trip term [20], which plays a role in explaining the flow transition from laminar to turbulent, while the previous WISE [19] used the Spalart-Allmaras model without the trip term. The Spalart-Allmaras model with a trip term is widely used in ANSYS Fluent (ANSYS Inc., 2017). It is because it offers higher computational stability and reliability compared to other turbulence models [6,51,52]. It has the advantage to predict the flow transition by designating the tripping points for two-dimensions or tripping lines for three-dimensions where the transition on-set positions are expected. However, the accuracy of the solution depends on the tripping points or lines selected by users. Therefore, there is an uncertainty that depends on user experience.

On the other hand, the previous version of WISE adopts the modified Spalart-Allmaras model, which includes a fully turbulent assumption with the surface roughness. Except for the trip term, the turbulent model of the previous WISE is identical to that of FENSAP-ICE. To reduce the uncertainty associated with the expertise of the users, the trip term is removed. As mentioned in the introduction section, flow transition has been observed in WISE as well as in the other study [22], even in the tip region. When our

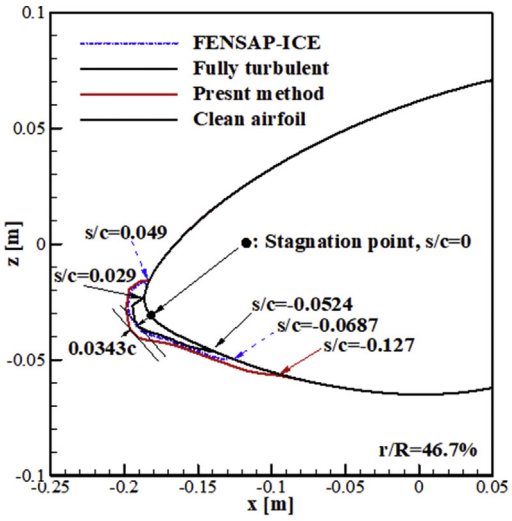

(a) $r/R = 46.7\%$

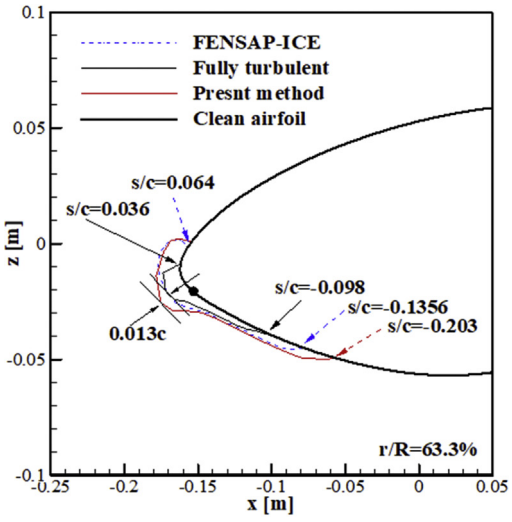

(b) $r/R = 63.3\%$

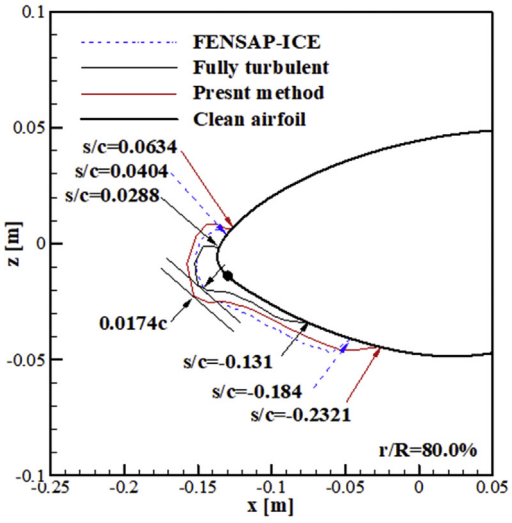

(c) $r/R = 80.0\%$

Fig. 6. Ice accretion shapes under glaze ice conditions; present method (thin red), fully turbulent [19] (thin black), and FENSAP-ICE [17] (dotted). (For interpretation of the references to colour in this figure legend, the reader is referred to the Web version of this article.)

new turbulent transitional model is applied, the ice accretion shapes agree well with FENSAP-ICE; WISE with the suggested transition model captures the basic flow perturbations induced by the roughness due to ice accretion, without need for specifying tripping points (or lines).

Our previous study [19] compared the rime ice accretion shapes obtained by FENSAP-ICE and WISE. The rime ice condition was applied while keeping the same icing and operating conditions of the present study, except for the temperature of −15 °C. In the rime ice condition, the previous study found no significant difference from the presently used glaze ice condition. It is well known that the local ice accretion rate is mainly controlled by the local convective heat transfer [53]. Thus the previous study emphasized improvement of the turbulence model, which can account for the flow transition induced by surface roughness since the local heat transfer rate is determined by the turbulence model.

To clearly show the reason for the improvement due to the application of the transitional turbulence model, distributions of heat transfer rate are plotted in Fig. 7. Over all sections of the blade, peaks of heat transfer coefficients predicted by the transition model exceed those from the fully-turbulent rough Spalart-Allmaras model. Knopp et al. [29] directly compared their method with the modified Spalart-Allmaras turbulence model [14]. The modified Spalart-Allmaras turbulence model consistently underestimated the skin friction on the various roughened flat plates compared to their method. It can be expected that the modified Spalart-Allmaras turbulence model predicts lower heat transfer rates compared to the present method (which employs the method suggested by Knopp et al. [29]), as thermal boundary layers behave analogously to momentum boundary layers in this application. As shown in Fig. 7, the present method applying the boundary condition proposed by Knopp et al. [29] yields a higher heat transfer rate than the modified Spalart-Allmaras turbulence model.

Because of the low convective cooling along the blade, the length of ice horns was unpredictable, and the runback water did not freeze sufficiently when the fully turbulent model was applied. In the results of the transition model, the second peaks on the upper surfaces can be observed. The locations of the second peak coincide with the icing limits on the upper surfaces. The high value of the second peak prevents the progression of the runback water. On the lower surface, the low-heat transfer rate is maintained before the transition onset. The runback water can flow along a wide range of lower surface.

4. Conclusion

This work aims to develop and improve the understanding and modeling of aerodynamic phenomena affecting turbine blades (or wings) that have experienced ice accretion. We extend the Langtry-Menter [21] turbulence transition model, coupled with a transport equation for roughness amplifier, by applying boundary conditions for turbulent kinetic energy (k) and specific dissipation rate (ω) suggested by Knopp et al. [29]; this allows prediction of flow transition and distributions of skin friction for a rough surface. To validate the present method, the distributions of skin friction coefficients and heat transfer for a roughened flat plate and circular cylinder are compared with numerical and experimental data. Finally, the modified transition model is applied within the aerodynamic module of a wind turbine icing simulation code. The ice accretion shapes obtained using both fully turbulent and modified transition models are compared.

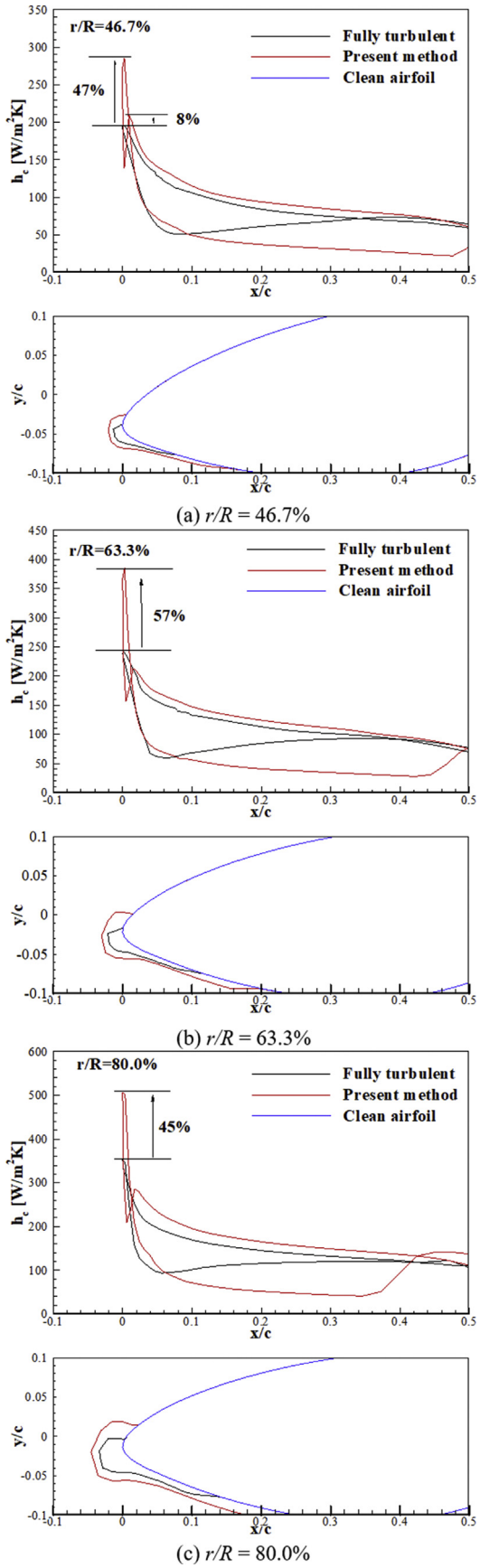

Fig. 7. Distributions of heat transfer rate (h_c) and ice accretion shapes; present method and fully turbulent [19].

Although the boundary conditions were originally designed for k-ω SST turbulence models to account for wall roughness under the assumption of fully developed turbulence, the distributions of skin friction and transition onset position of the present method match well with experimental results. In particular, the present method shows a significant improvement in the peak value of skin friction on the circular cylinder. Since the blending functions of k and ω prevent the growth of k and μ_t in laminar regions which have a significant viscous sublayer, the latter does not significantly affect the prediction of the flow transition. Since the value of k at the wall, which was always treated as 0 in the previous studies, was corrected to be close to the log-layer value, more accurate k and μ_t could be predicted for the fully roughened surface.

The present method overpredicts the distributions of skin friction in the low Reynolds condition, where the flow remains laminar. The Langtry-Menter transition model [21] coupled with a transport equation for roughness amplifier is corrected for the flow transition. The roughness amplifier tends to maintain the high value of intermittency, even in laminar regions. To improve the accuracy of the present method for low Reynolds number conditions, it is necessary to modify not only the boundary conditions, but also the transport equation for roughness amplifier.

Our extended RANS turbulence model implementation, which can consider the flow transition induced by surface roughness, is applied for wind turbine icing simulation. The newly modified model can more accurately predict ice accretion shapes at various sections, compared to the fully turbulent model. The icing limits of WISE on both upper and lower surfaces are well-matched with those of FENSAP-ICE, which uses the trip term that can explain the flow transition. The present turbulent model exhibits the advantage that it provides a consistent result, without needing to be tuned by the user.

The newly updated turbulent model is applied for wind turbine icing. Since this newly modified turbulent model can be generalized to various problems that require consideration of the flow transition induced by surface roughness, it is expected to be used not only for icing but also for attachment of insects and/or dust, and surface erosion.

CRediT authorship contribution statement

Chankyu Son: Conceptualization, Software, Methodology, Formal analysis, Writing - original draft. **Mark Kelly:** Writing - review & editing; theoretical oversight. **Taeseong Kim:** Writing - review & editing, Validation, Investigation, Resources, Supervision, Funding acquisition.

Declaration of competing interest

The authors declare that they have no known competing financial interests or personal relationships that could have appeared to influence the work reported in this paper.

Acknowledgment

The research leading to these results has received funding from the European Union's Horizon 2020 research and innovation programme under the Marie Skłodowska-Curie grant (EU) agreement no. 713683 (COFUNDfellowsDTU), this work was also conducted under framework of the research and development program of the Korea Institute of Energy Research (C0-2453), and the co-authors would like to acknowledge financial support under the Danish EUDP support scheme for project IEA Task 19 (grant no. 64019-0515).

References

[1] R.B. Langtry, A correlation-based transition model using local variables for unstructured parallelized CFD codes, J. Turbomach. 128 (2006) 413, https://doi.org/10.1115/1.2184352.
[2] J. Shin, Characteristics of surface roughness associated with leading-edge ice accretion, J. Aircraft 33 (1996) 316–321, https://doi.org/10.2514/3.46940.
[3] N. Dalili, A. Edrisy, R. Carriveau, A review of surface engineering issues critical to wind turbine performance, Renew. Sustain. Energy Rev. (2009), https://doi.org/10.1016/j.rser.2007.11.009.
[4] B. Zohuri, Similitude Theory and Applications. Galaxy Adv. Eng., Springer International Publishing, 2015, pp. 93–193, https://doi.org/10.1007/978-3-319-13476-5_2.
[5] L. Shu, J. Liang, Q. Hu, X. Jiang, X. Ren, G. Qiu, Study on small wind turbine icing and its performance, Cold Reg. Sci. Technol. 134 (2017) 11–19, https://doi.org/10.1016/j.coldregions.2016.11.004.
[6] R. Hann, R.J. Hearst, L. Sætran, T. Bracchi, Experimental and numerical icing penalties of a S826 airfoil at low Reynolds numbers, Aerospace (2020) 1–18, https://doi.org/10.3390/aerospace7040046.
[7] A. Sayigh, D. Milborrow, The Age of Wind Energy: Progress and Future Directions from a Global Perspective, Springer, Switzerland, 2020, https://doi.org/10.1007/978-3-030-26446-8.
[8] D.N. Anderson, J.-C. Tsao, Overview of icing physics relevant to scaling. https://doi.org/10.4271/2003-01-2130, 2005.
[9] W.B. Wright, R.W. Gent, D. Guffond, DRA/NASA/ONERA collaboration on icing research, Part II-prediction of airfoil ice accretion, NASA Contract Rep 202349 (1997) 1–50.
[10] H. Schlichting, K. Gersten, Boundary-layer theory, Boundary-Layer Theory 1–799 (2016), https://doi.org/10.1007/978-3-662-52919-5.
[11] F.M. White, Viscous Fluid Flow, third ed., McGraw-Hill, NewYork, 2005.
[12] E. Albert, von Doenhoff, E.A. Horton, A Low-Speed Experimental Investigation of the Effect of a Sandpaper Type of Roughness on Boundary-Layer Transition, 1956.
[13] J. Nikuradse, Laws of Flow in Rough Pipes, 1950. Washington.
[14] B. Aupoix, P.R. Spalart, Extensions of the Spalart - allmaras turbulence model to account for wall roughness, Int. J. Heat Fluid Flow 24 (2003) 454–462, https://doi.org/10.1016/S0142-727X(03)00043-2.
[15] P.R. Spalart, S.R. Allmaras, J. Reno, One-Equatlon Turbulence Model for Aerodynamic Flows. 30th Aerosp. Sci. Meet. Exhib., AIAA, Reno, NV, 1992, p. 23, https://doi.org/10.2514/6.1992-439.
[16] F.R. Menter, Two-equation eddy-viscosity turbulence models for engineering applications, AIAA J. 32 (1994) 1598–1605, https://doi.org/10.2514/3.12149.
[17] T. Reid, G. Baruzzi, I. Ozcer, D. Switchenko, W. Habashi, Fensap - ICE simulation of icing on wind turbine blades , Part 1 : performance degradation, 51st AIAA Aerosp Sci Meet Incl New Horizons Forum Aerosp Expo 07 - 10 January 2013 (2013) 1–18, https://doi.org/10.2514/6.2013-750. Grapevine (Dallas/Ft Worth Reg Texas.
[18] P. Verdin, F. Charpin Jp, C.P. Thompson, Multistep results in ICECREMO2, J. Aircraft 46 (2009) 1607–1613, https://doi.org/10.2514/1.41451.
[19] C. Son, T. Kim, Development of an icing simulation code for rotating wind turbines, J. Wind Eng. Ind. Aerod. 203 (2020) 104239, https://doi.org/10.1016/j.jweia.2020.104239.
[20] B. Héloïse, F. Morency, W.G. Habashi, P. Benquet, Roughness implementation in FENSAP-ICE: model calibration and influence on ice shapes, J. Aircraft 40 (2003) 1212–1215, https://doi.org/10.2514/2.7214.
[21] R.B. Langtry, F.R. Menter, Correlation-based transition modeling for unstructured parallelized computational fluid dynamics codes, AIAA J. 47 (2009) 2894–2906, https://doi.org/10.2514/1.42362.
[22] F.R. Menter, R. Langtry, S. Völker, S. Völker, Transition modelling for general purpose CFD codes, Flow, Turbul. Combust. 77 (2006) 277–303, https://doi.org/10.1007/s10494-006-9047-1.
[23] P. Dassler, D. Kozulovic, A. Fiala, Modeling of roughness induced transition using local variables, in: J.C.F. Sequeira, A P (Eds.), Lisbon, Portugal: V European Conference on Computational Fluid Dynamics, 2010.
[24] C.M. Langel, R. Chow, C.P. van Dam, D. Maniaci, R.S. Ehrmann, E.B. White, A computational approach to simulating the effects of realistic surface roughness on boundary layer transition, AIAA Aerosp Sci Meet - AIAA Sci Technol Forum Expo SciTech (2014) 1–16, 2014.
[25] D.C. Wilcox, Reassessment of the scale-determining equation for advanced turbulence models, AIAA J. 26 (1988) 1299–1310, https://doi.org/10.2514/3.10041.
[26] V.C. Patel, J.Y. Yoon, Application of turbulence models to separated flow over rough surfaces, J Fluids Eng Trans ASME 117 (1995) 234–241, https://doi.org/10.1115/1.2817135.
[27] A. Hellsten, S. Laine, A. Hellsten, S. Laine, Extension of the k-omega-SST turbulence model for flows over rough surfaces, 22nd Atmos Flight Mech Conf (1997) 252–260, https://doi.org/10.2514/6.1997-3577.
[28] P.A. Durbin, G. Medic, J.M. Seo, J.K. Eaton, S. Song, Rough wall modification of two-layer k-ε, J Fluids Eng Trans ASME 123 (2001) 16–21, https://doi.org/10.1115/1.1343086.
[29] T. Knopp, B. Eisfeld, J.B. Calvo, A new extension for k– turbulence models to account for wall roughness, Int. J. Heat Fluid Flow 30 (2009) 54–65, https://doi.org/10.1016/j.ijheatfluidflow.2008.09.009.
[30] B. Aupoix, Wall roughness modelling with k-w STT model, in: 10th Int. ERCOFTAC Symp. Eng. Turbul. Model. Meas, 2014. MARBELLA, Spain.
[31] C. Zhu, B. Fu, Z. Sun, C. Zhu, 3D ice accretion simulation for complex configuration basing on improved messinger model, Int J Mod Phys Conf Ser 19 (2012) 341–350, https://doi.org/10.1142/S2010194512008938.
[32] P. Fu, M. Farzaneh, A CFD approach for modeling the rime-ice accretion process on a horizontal-axis wind turbine, J. Wind Eng. Ind. Aerod. 98 (2010) 181–188, https://doi.org/10.2147/VHRM.S39726.
[33] L. Hu, X. Zhu, J. Chen, X. Shen, Z. Du, Numerical simulation of rime ice on NREL Phase VI blade, J. Wind Eng. Ind. Aerod. 178 (2018) 57–68, https://doi.org/10.1016/j.jweia.2018.05.007.
[34] C. Son, S. Oh, K. Yee, Ice accretion on helicopter fuselage considering rotor-wake effects, J. Aircraft 54 (2017) 500–518, https://doi.org/10.2514/1.C033830.
[35] C. Son, K. Yee, Procedure for determining operation limits of high-Altitude long-Endurance aircraft under icing conditions, J. Aircraft 55 (2018) 294–309, https://doi.org/10.2514/1.C034490.
[36] N. Davis, A.N. Hahmann, N.E. Clausen, M. Žagar, Forecast of icing events at a wind farm in Sweden, J Appl Meteorol Climatol 53 (2014) 262–281, https://doi.org/10.1175/JAMC-D-13-09.1.
[37] J. Huang, A simple accurate formula for calculating saturation vapor pressure of water and ice, J Appl Meteorol Climatol 57 (2018) 1265–1272, https://doi.org/10.1175/JAMC-D-17-0334.1.
[38] A. Hellsten, S. Laine, Extension of the K-ω-SST Turbulence Model for Flows over Rough Surfaces. 22nd Atmos. Flight Mech. Conf., American Institute of Aeronautics and Astronautics, Reston, Virigina, 1997, pp. 252–260, https://doi.org/10.2514/6.1997-3577.
[39] P.M. Ligrani, R.J. Moffat, Structure of transitionally rough and fully rough turbulent boundary layers, J. Fluid Mech. 162 (1986) 69–98, https://doi.org/10.1017/S0022112086001933.
[40] C. Colebrook, C.M. White, Experiments with fluid friction in roughened pipes, Proc R Soc London Ser A - Math Phys Sci 161 (1937) 367–381, https://doi.org/10.1098/rspa.1937.0150.
[41] P.R. Spalart, Trends in turbulence treatments, AIAA Pap 2000-2306 Fluids 2000 Conf Exhib 39 (2000) 1–13, https://doi.org/10.2514/MFDC00.
[42] A. Zanon, M. De Gennaro, H. Kühnelt, Wind energy harnessing of the NREL 5 MW reference wind turbine in icing conditions under different operational strategies, Renew. Energy 115 (2018) 760–772, https://doi.org/10.1016/j.renene.2017.08.076.
[43] E.G. Feindt, Untersuchungen über die Abhängigkeit des Umschlages laminar-turbulent von der Oberflächenrauhigkeit und der Druckverteilung, Technische Hochschule Carolo-Wilhelmina zu Braunschweig, 1957.
[44] E. Achenbach, Total and local heat transfer from a smooth circular cylinder in cross-flow at high Reynolds number, Int. J. Heat Mass Tran. 18 (1975) 1387–1396, https://doi.org/10.1016/0017-9310(75)90252-5.
[45] E. Achenbach, The effect of surface roughness on the heat transfer from a circular cylinder to the cross flow of air, Int. J. Heat Mass Tran. 20 (1977) 359–369, https://doi.org/10.1016/0017-9310(77)90157-0.
[46] E. Achenbach, Influence of surface roughness on the cross-flow around a circular cylinder, J. Fluid Mech. 46 (1971) 321–335, https://doi.org/10.1017/S0022112071000569.
[47] F. Chedevergne, B. Aupoix, Accounting for Wall Roughness Effects in Turbulence Models: a Wall Function Approach, 7th EUCASS Conf, 2017, https://doi.org/10.13009/EUCASS2017-372.
[48] A. Prakash, E. Laurendeau, Consistent surface roughness extension for wall functions, Int. J. Heat Fluid Flow (2020), https://doi.org/10.1016/j.ijheatfluidflow.2020.108552.
[49] G.A. Ruff, B.M. Berkowitz, Users Manual for the NASA Lewis Ice Accretion Prediction Code, LEWICE, 1990.
[50] W. Wright, User's Manual for LEWICE Version 3.2, Nasa/Cr-2008-214255, 2008, 20080048307.
[51] N. Fajt, R. Hann, T. Lutz, The Influence of Meteorological Conditions on the Icing Performance Penalties on a UAV Airfoil, 8th Eur Conf Aeronaut Sp Sci, 2019.
[52] X. Bu, G. Lin, X. Shen, Z. Hu, D. Wen, Numerical simulation of aircraft thermal anti-icing system based on a tight-coupling method, Int. J. Heat Mass Tran. 148 (2020) 119061, https://doi.org/10.1016/j.ijheatmasstransfer.2019.119061.
[53] R. John Hansman, K. Yamaguchi, B. Berkowitz, M. Potapczuk, Modeling of surface roughness effects on glaze ice accretion, J. Thermophys. Heat Tran. 5 (1991) 54–60, https://doi.org/10.2514/3.226.

Nomenclature

A_r: = roughness amplifier
β_k: = constant in the k-ω model, 0.09
c_f: = skin friction coefficient ($\tau_w/0.5\rho U_\infty^2$)
C_p: = specific heat capacity
c_p: = pressure coefficient
D: = cylinder diameter, 0.15m
Δu: = magnitude shift in the logarithmic speed profile
Fro: = Frossling number ($Nu/\sqrt{Re}$)
γ: = intermittency parameter [dimensionless]
h_c: = heat convection coefficient, W/m$^2\cdot$K
h_f: = height of water film, m
k: = specific turbulent kinetic energy, m^2/s^2
κ: = von Kármán constant

k_s: = surface roughness, m
k_s^+: = non-dimensional sand-grain roughness ($\sqrt{\tau_w/\rho} \cdot k_s/\nu$)
L_{fus}: = latent heat of fusion, 334 kJ/kg
L_{vap}: = latent heat of vaporization, 2270 kJ/kg
LWC: = liquid water content, g/m^3
MVD: = median volume diameter, μm
μ: = viscosity, Pa·s
$\dot{m}_{com}$: = impinging water rate, $kg/s{\cdot}m^2$
$\dot{m}_{ice}$: = accumulated ice rate, kg/s·m^2
$\dot{m}_{eva}$: = evaporative mass, kg/s·m^2
ν: = kinematic viscosity, μ/ρ
Nu: = Nusselt number
Pr: = Prandtl number
ω: = specific dissipation rate, 1/s
R: = rotor radius, m
r: = sectional radius, m
s: = distance from a stagnation point, m
Re: = Reynolds number
Re_{θ_t}: = transition onset momentum-thickness Reynolds number (based on free-stream conditions)
$\tilde{R}e_{\theta_t}$: = transition onset momentum-thickness Reynolds number (obtained from a transport equation)
ρ: = density, kg/m^3
t: = time, s
T: = temperature, K
$\bar{T}_{eq}$: = equilibrium temperature, C
$\overrightarrow{\tau}_w$: = shear stress on the water film from air, Pa
$\overline{U}_f$: = mean velocity vector of water film, m/s
V: = volume, m^3

subscript

a: = air properties, absolute frame
d: = droplet properties
e: = edge of boundary layer
i: = ice properties
∞: = freestream properties
k: = group of droplet diameter
l: = laminar
sat: = saturated condition
t: = turbulent